Resonance three-Photon Ionization of Atomic Mn using Ti:Sapphire Lasers in a Hot Cavity Laser Ion Source*

Y. Liu[1], T. Gottwald[2], C. Mattolat[2], K. Wendt[2]

[1]*Physic Division, Oak Ridge National Laboratory, Oak Ridge, TN 37831, USA*
[2]*Institut für Physik, Johannes Gutenberg Universität Mainz, D-55128 Mainz, Germany*

Abstract

Three-photon resonance ionization of atomic Mn in a hot cavity ion source using Ti:sapphire lasers has been demonstrated. Three-step ionization schemes employing different intermediate levels and Rydberg and autoionizing states in the final ionization step are established. Strong autoionizing resonances were observed via the $3d^5 4s5s\ f\ ^6S_{5/2}$ level at 49415.35 cm^{-1}, while Rydberg transitions were reached from the $3d^5 4s4d\ e\ ^6D_{9/2,7/2,5/2}$ levels at around 47210 cm^{-1}. Analyses of the strong Rydberg transitions associated with the $3d^5 4s4d\ e\ ^6D_{7/2}$ lower level indicate that they belong to the dipole-allowed $4d \rightarrow nf\ ^6F^\circ_{9/2,7/2,5/2}$ series converging to the $3d^5 4s\ ^7S_3$ ground state of Mn II. From this series, an ionization potential of 59959.56 ± 0.01 cm^{-1} is obtained for Mn. At high ion source temperatures the semi-forbidden $4d \rightarrow nf\ ^8F^\circ_{9/2,7/2,5/2}$ series was also observed. The overall ionization efficiency for Mn has been measured to be about 0.9% when using the strong AI transition in the third excitation step and 0.3% when employing an intense Rydberg transition. Experimental data indicate that the ionization efficiency was limited by the interaction of Mn atoms with ion source materials at high temperatures.

1. Introduction

Beams of radioactive Manganese (Mn) isotopes are needed for experimental studies in nuclear physics and material science. Various Mn isotopes are used for spectroscopy studies to elucidate the evolution of nuclear shell structure in exotic nuclei across the $N = 28$ ($^{50-56}$Mn) [1] and $N = 40$ ($^{61-69}$Mn) [2] closed neutron shells. Neutron-rich $^{57-66}$Mn isotopes are the object for high-precision mass measurements probing the existence of a newly postulated island of inversion around the N = 40 shell closure region [3,4]. Short-lived ^{61}Mn isotope has also been utilized to obtain ^{71}Fe that is more difficult to produce [5]. These experiments are of fundamental interest in validating the predictions of the nuclear shell model far from stability. Mn-57 is an important probe nucleus for Mössbauer spectroscopy of implanted impurities in solids [6-8], which is a powerful tool to investigate the properties and dynamical behavior of dilute impurities in materials. Isotopes of $^{56-61}$Mn are of particular interest for emission channeling lattice location measurements of transition metals in dilute magnetic semiconductors [8-12] in order to understand the ferromagnetism in these materials with promising applications in the upcoming field of spintronics.

The majority of these studies require an intense and isobarically pure ion beam of Mn radioisotopes. These are produced dominantly using the isotope separation on-line (ISOL) technique with

a resonant ionization laser ion source (RILIS) [6] and recently also by the in-flight isotope separation method [7]. In a RILIS, atomic species are stepwise excited by laser radiation, leading to ionization in the last transition. The process consists of two or three resonant steps, so that it is chemically selective and efficient. Correspondingly, the RILIS ensures the generation of isobarically and isotopically pure ion beams at the subsequent isobar separator. To date, as for many other elements, RILIS is the primary ion source for the production of pure radioactive Mn ion beams at ISOL facilities [13].

Resonant ionization of Mn in a RILIS has been obtained initially using the combination of dye and copper vapor lasers [6], the latter being today replaced by Nd:YAG lasers [14]. Three-photon ionization schemes involving two resonant excitation and a subsequent non-resonant ionization step were applied. Other laser ionization schemes studied in Ref [15] are also specific to dye and Nd:YAG lasers. In this paper we report the first three-photon ionization of Mn using tunable Ti:sapphire lasers and involving three resonant steps. The impetus of this work comes from the increasing use of Ti:sapphire lasers for RILIS applications at ISOL facilities around the world [16-19] and the corresponding need for excitation and ionization schemes for atomic Mn exclusively using Ti:sapphire lasers. In particular, at the Holifield Radioactive Ion Beam Facility (HRIBF), Oak Ridge National Laboratory, a RILIS employing three Ti:sapphire lasers has recently been commissioned [17]. We will present the three-step, three-photon resonant ionization schemes investigated and the spectroscopic studies of the Rydberg and autoionizing states in Mn. The laser power requirements and ionization efficiencies for different ionization schemes will also be discussed.

2. Experimental Setup

The experiment was conducted with a hot cavity RILIS at the off-line Ion Source Test Facility 2 (ISFT2) of HRIBF at ORNL. The experimental apparatus and the RILIS have been previously reported [20,21]. Briefly, the RILIS consisted of an ion source unit with a 3-mm diameter and 30-mm long cavity and a system of three tunable Ti:Sapphire lasers. The cavity was resistively heated by a DC electric current to high temperatures, typically exceeding 2000 K. A graphite target reservoir was connected to the hot cavity via a hot transfer tube and was radiatively heated by a separate Ta heater surrounding the reservoir. Solid Mn metal samples were heated in the target reservoir to release gaseous Mn atoms which effused towards the hot cavity and were ionized by laser radiation. The ions were extracted from the ion source, accelerated to 20 kV to form a collimated ion beam, and directed to a 90° sector field dipole magnet for mass separation. The intensity of mass-selected ^{55}Mn ions was measured after the dipole magnet with a Faraday cup detector. In addition, the total ion intensity extracted from the ion source could be monitored with a Faraday cup before the magnet.

The laser system consisted of three Ti:sapphire lasers jointly pumped by a pulsed frequency-doubled Nd:YAG laser operating at a repetition rate of 10 kHz. Two of the lasers were developed at and provided by the University of Mainz. They generated tunable laser light from 690-960 nm with average power up to 5 W at peak wavelengths of the tuning curve. Detailed information on the Mainz lasers is available in [22]. The third laser was a commercial Ti:sapphire laser (Photonics Industries International Bohemia, New York) with a diffraction grating for continuous wavelength tuning between 720-940 nm. It provided up to 2 W maximum power at about 810 nm. A frequency conversion unit was also provided by Mainz for frequency doubling and tripling of the fundamental output of the Mainz lasers. The Ti:sapphire laser outputs had pulse widths on the order of 30 ns and were synchronized to better than 5 ns with internal Pockels cells. The spectral line widths of the lasers were 3-5 GHz.

All lasers were located on a laser table located behind the dipole magnet at a distance of about 4 m from the ion source unit. Laser beams from the three Ti:sapphire lasers were merged into one beam on the optical table, which was sent into the experimental apparatus under vacuum through a 45-degree window attached to the dipole magnet in straight view of the ion source assembly and was focused into the 3-mm-diameter hot cavity of the ion source. Inside the beam line, the laser beam counterpropagated collinearly

with the ion beam. The wavelengths of the three laser outputs were monitored simultaneously using a calibrated wavelength meter (HighFinesse WS6) equipped with a 4-channel opto-mechanical switcher. The wavelength readings were found to be slightly varying on the order of 0.05 cm^{-1}, with different spatial couplings of the identical laser beam into the wavelength meter. This uncertainty was considered as a systematic error for the measured laser wavelengths.

3. Results and discussion

3.1 Ionization schemes

Three-photon, three-step resonant ionization schemes for Mn with all Ti:sapphire lasers were investigated in this work. For the first step, transitions from the $3d^54s^2$ $a\ ^6S_{5/2}$ ground state to the $3d^54s4p$ $y\ ^6P^o_J$ with J = 3/2, 5/2 or 7/2 excited states were used, for which frequency-tripled photons at λ_1 = 280.106, 279.827 and 279.482 nm, respectively, were required. These three first-step transitions have already been studied by Fedoseyev et al., using frequency doubled dye laser radiation [6]. Suitable second steps for Ti:sapphire laser excitation were determined according to the available wavelength and power. Using the NIST Atomic Spectra Database [23], we selected the $3d^54s5s$ $f\ ^6S_J$ with J = 5/2 state at 49415.35 cm^{-1} and the $3d^54s4d$ $e\ ^6D_J$ with J = 5/2, 7/2 and 9/2 states at 47207.28 cm^{-1}, 47212.06 cm^{-1}, and 47215.61 cm^{-1}, respectively, as the upper levels. These could be populated in the second excitation with near infrared photons in the range of 728 nm up to 874 nm. Radiation in this range was directly generated as Ti:sapphire laser fundamental output. Spectroscopic investigation was necessary to identify suitable atomic transitions for resonant ionization in the third step. In the photoionization spectra obtained by scanning the third laser wavelength, a number of high-lying Rydberg levels below the first ionization potential (IP) as well as some autoionizing (AI) levels were observed. As illustrated in Fig. 2, Mn atoms can be resonantly excited to one of those Rydberg levels from the intermediate $3d^54s4d$ $e\ ^6D_J$ with J =5/2, 7/2 and 9/2 state and subsequently ionized by black-body radiation or collisions, or excited to an AI level above the IP from the intermediate $3d^54s5s$ $f\ ^6S_{5/2}$ state. Both pathways could be at least one to two orders of magnitude more efficient than non-resonant ionization.

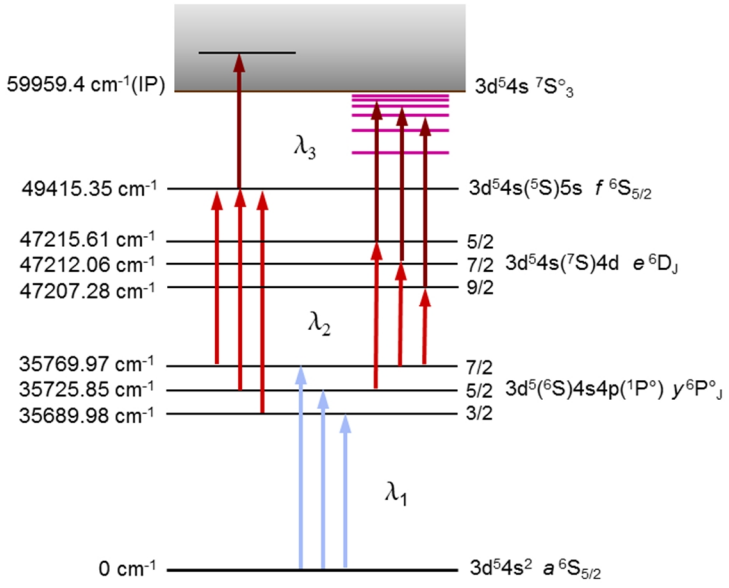

Figure 1. Schematic diagram of the three-photon, three-step excitation schemes investigated for Mn, showing the intermediate levels and the Rydberg and autoionizing resonances approached via different intermediate levels.

The intermediate state energies shown in Fig. 1 were taken from Ref. [23]. Before extracting spectroscopic information out of the Rydberg and AI states observed, we examined these energies by studying the line profiles of the corresponding resonant transitions. The resonance spectrum of a transition was obtained by measuring the ion intensity as a function of the excitation laser wavelength over the region of resonance while keeping the wavelengths of the other two lasers fixed. The center of gravity and the full width at half maximum (FWHM) of the transition were obtained by fitting the experimental data to an appropriate line shape function. Figure 2 illustrates the measured resonance spectra of two first-step transitions. Figure 2(a) corresponds to the $a\ ^6S_{5/2} \rightarrow y\ ^6P^o_{7/2}$ excitation, which exhibits a Voigt line shape. It is fitted using an approximated Voigt function given by a linear combination of Lorentzian and Gaussian line shapes [24,25]

$$V(E) = A\,[r \cdot L(E) + (1-r)G(E)] + I_0 \tag{1}$$

$$L(E) = \frac{2}{\pi w}\frac{1}{1 + 4\,(\frac{E-E_c}{w})^2} \tag{2}$$

$$G(E) = \frac{2}{w}\sqrt{\frac{\ln 2}{\pi}}\exp[-4\ln 2\,(\frac{E-E_c}{w})^2]\,, \tag{3}$$

where L(E) and G(E) are normalized Lorentzian and Gaussian functions, respectively, with an equal FWHM of w, E is the laser photon energy, E_c is the center of gravity of the resonance, A is an amplitude parameter, r is a parameter describing the relative contributions of L(E) and G(E), and I_0 represents the ion intensity not resulting from the three-step photoionization process. The FWHM of the approximated Voigt function is also equal to w. The fitted Voigt profile is shown in Fig. 2(a) as solid line. Figure 2(b) shows the $a\ ^6S_{5/2} \rightarrow y\ ^6P^o_{5/2}$ excitation, which is better described by a saturated Gaussian profile

$$I(E) = I_0 + A\frac{S\cdot\exp[-\frac{(E-E_C)^2}{2w^2}]}{S\cdot\exp\left[-\frac{(E-E_C)^2}{2w^2}\right]+1}\quad, \tag{4}$$

where $I(E)$ is ion intensity at photon energy E, E_c, A, and I_0 are similar to those for Eqs. (1)-(3), w is the line width of the Gaussian component, and S is a saturation parameter. The solid line in Fig. 2(b) is a fit to Eq. (4). The second-step transitions studied are found to fit well by the saturated Gaussian profile with FWHM on the order of 20 GHz, which suggests that these transitions were well saturated and significantly power broadened under our experimental conditions.

Table 1 gives the centroid energies (E_c) of the intermediate states determined from the experimental resonance spectra. The energy of the second intermediate states is given as $E_c(\lambda_1) + E_c(\lambda_2)$, where $E_c(\lambda_1)$ and $E_c(\lambda_2)$ are the center of gravity of the first and second excitations, respectively. For comparison, the previously established energies of these states from Ref. [23] are given in column 3. Column 4 is the first and second excitation transitions used and column 5 is the fitted FWHM of the corresponding transitions. As shown, the FWHM of the second-step transitions is much larger than that of the first excitations. The experimental energies are in good agreement with the literature values. Consequently, we have used the more precise literature values for these states in subsequent spectroscopy studies.

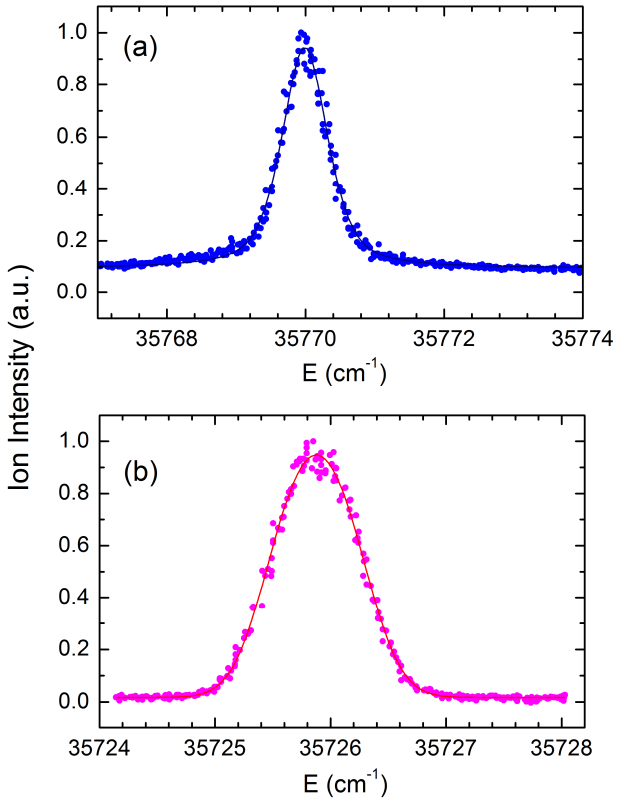

Figure 2. Spectral profiles of (a) $a\ ^6S_{5/2} \rightarrow y\ ^6P^o_{7/2}$ excitation and (b) $a\ ^6S_{5/2} \rightarrow y\ ^6P^o_{5/2}$ excitation. The solid lines are fitted line-profiles: (a) Voigt profile with E_0 = 35769.99(2) and FWHM = 8.1(1) GHz; (b) saturated Gaussian profile with E_0 = 35725.88(1) and FWHM = 9.2(2) GHz.

Table 1. Centroid energies of the intermediate states determined in this study and the literature values [23], and the FWHM of the excitation transitions.

State	Expt. E_c (cm^{-1})	Lit. E (cm^{-1})	Transition	FWHM (GHz)
$3d^54s4p\ \ y\ ^6P^o_{3/2}$	35690.02(1)	35689.98	$a\ ^6S_{5/2} \rightarrow y\ ^6P^o_{3/2}$	7.8(1)
$3d^54s4p\ \ y\ ^6P^o_{5/2}$	35725.88(1)	35725.85	$a\ ^6S_{5/2} \rightarrow y\ ^6P^o_{5/2}$	9.1(2)
$3d^54s4p\ \ y\ ^6P^o_{7/2}$	35769.99(2)	35769.97	$a\ ^6S_{5/2} \rightarrow y\ ^6P^o_{7/2}$	8.1(1)
$3d^54s4d\ e\ ^6D_{7/2}$	47212.11(7)	47212.06	$y\ ^6P^o_{7/2} \rightarrow e\ ^6D_{7/2}$	22(1)
$3d^54s4d\ e\ ^6D_{5/2}$	47215.64(1)	47215.61	$y\ ^6P^o_{5/2} \rightarrow e\ ^6D_{5/2}$	23(3)
$3d^54s5s\ \ f\ ^6S_{5/2}$	49415.41(3)	49415.35	$y\ ^6P^o_{5/2} \rightarrow f\ ^6S_{5/2}$	24(2)

3.2 Rydberg Series

Rydberg levels were observed via the $3d^54s4d\ \ e\ ^6D_J$ states with J = 5/2, 7/2 and 9/2 as the lower levels in the third step (the excitation paths on the right in Fig. 1). Due to limited experimental time, only the Rydberg spectra associated with the J = 7/2 lower level at 47212.06 cm^{-1} were measured with fine

resolution. Figure 3 shows a photoionization spectrum obtained by using the excitation sequence $a\ ^6S_{5/2} \rightarrow y\ ^6P^o_{7/2} \rightarrow e\ ^6D_{7/2}$ for the first two steps and by scanning the third laser wavelength. The spectrum contains a well-developed Rydberg series converging to the ground state $3d^54s\ a\ ^7S_3$ of the ion Mn II. Rydberg series originating from the $3d^54s4d\ e\ ^6D_{7/2}$ state are correspondingly expected to belong to the $3d^54s\ (^7S)np$ or $3d^54s\ (^7S)nf$ configurations. In LS coupling scheme, the electric dipole-allowed terms are $^6P°_{7/2,5/2}$ for the *np* configuration and $^6F°_{9/2,7/2,5/2}$ for the *nf* configuration. Rydberg levels of $3d^54s\ (^7S)np\ ^6P°_{7/2,5/2,3/2}$ (n = 6-41) and $3d^54s\ (^7S)np\ ^8P°$ (n = 6-22) excited from the $3d^54s^2\ ^6S°_{5/2}$ ground state have been reported [26]. The energy positions of the observed series in Fig. 3 were slightly lower than those of the previously characterized $np\ ^6P°_{7/2,5/2,3/2}$ series. In addition, the $14p\ ^6P°_{7/2}$ and $^6P°_{5/2,3/2}$ splitting, known to be about 0.5 cm^{-1}[26], was not observed in the corresponding member of the present series. Hence, we have assigned the observed series to $nf\ ^6F°_{9/2,7/2,5/2}$ (n = 12-47) with multiplet splittings unresolved. The assignment of the principal quantum number for the *nf* series is based on the assumption that the quantum defect of the *nf* series is less than 1. This is supported by the observation that the quantum defects of the known $3d^54s\ (^7S)5f\ v\ ^6F°_J$ states for all J = 3/2 – 11/2 are on the order of 0.04 [23].

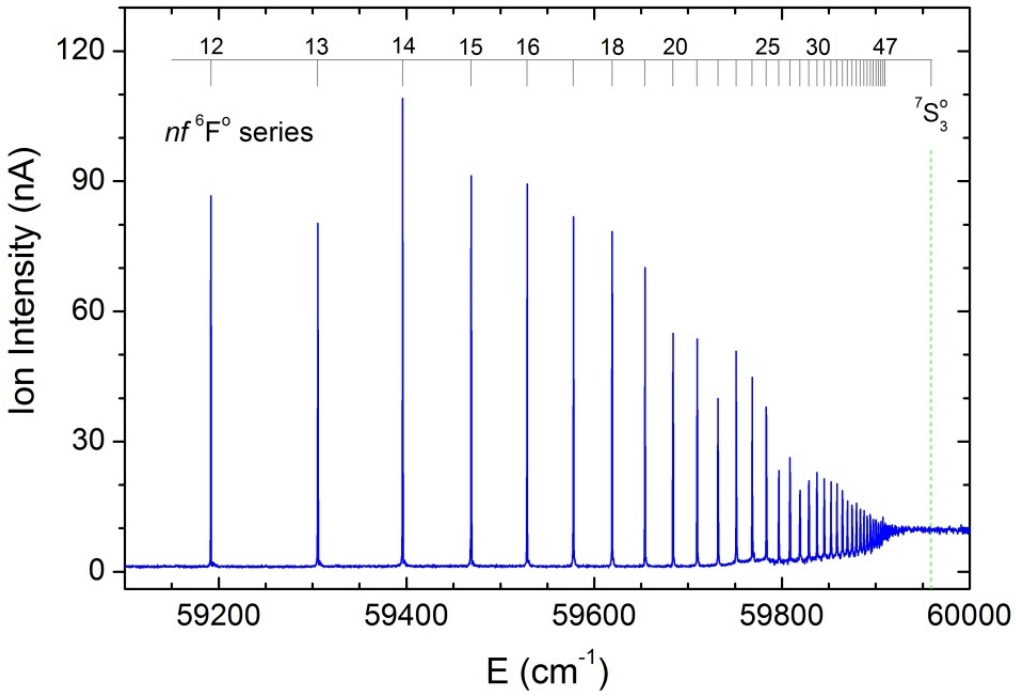

Figure 3. Rydberg spectrum obtained using the excitation sequence $a\ ^6S_{5/2} \rightarrow y\ ^6P^o_{7/2} \rightarrow e\ ^6D_{7/2}$ for the first two steps. The Rydberg states were excited by the third laser from the $e\ ^6D_{7/2}$ state. The spectrum is plotted as a function of the total energy. The vertical dashed line marks the position of the series convergence limit $^7S^o_3$, which is the ground state of Mn II.

The convergence limit of the $3d^54s(^7S)\ nf\ ^6F°_{9/2,7/2,5/2}$ Rydberg series was determined by fitting the experimental energy levels to the Rydberg-Ritz formula [27]

$$E_n = E_{limit} - \frac{R_M}{[n-\delta(n)]^2} \quad (5)$$

$$\delta(n) = A + \frac{B}{(n-A)^2} \quad (6)$$

where E_n is the total energy of the Rydberg level with principal quantum number n, E_{limit} the series converging limit, R_M = 109736.2199 cm^{-1} the mass corrected Rydberg constant for ^{55}Mn, $\delta(n)$ is the

quantum defect given by the Ritz expansion to the second order, and A and *B* are constants. The centroid energies of the Rydberg transitions were determined by fitting of individual Gaussian line profiles. The total energies of the Rydberg levels were obtained by adding the corresponding third photon energies to the energy of the $3d^5 4s4d\ e\ ^6D_{7/2}$ state. There were three separate measurements of the photoionization spectrum, each obtained by scanning the third laser wavelength over the same spectral region with a wavelength step width of about 0.25 cm^{-1}. The final E_n values were the average values of the three measurements. The uncertainties for the determined energy positions were on the order of 0.3 cm^{-1}, which included statistical errors and the systematic error of 0.1 cm^{-1} from the wavelength meter. Figure 6 shows the Rydberg-Ritz fit for the *nf* $^6F^\circ$ series, which gave E_{limit} = 59959.56 ± 0.01 cm^{-1} and A = 0.0546 ± 0.0005. The E_{limit} value corresponds to the IP of neutral Mn and is in close agreement with the previously reported value of 59959.40 ± 0.10 cm^{-1} [26], enhancing its precision by about a factor of ten. Table 2 lists the experimental and fitted energies and $\delta(n)$ values for the *nf* $^6F^\circ$ (*n* = 12-47) states. As discussed in detail e.g. in [21], the trend of increasing $\delta(n)$ values as *n* increases strongly confirms the assignment of a *nf* series instead of a *np* series, which would lead to a decrease.

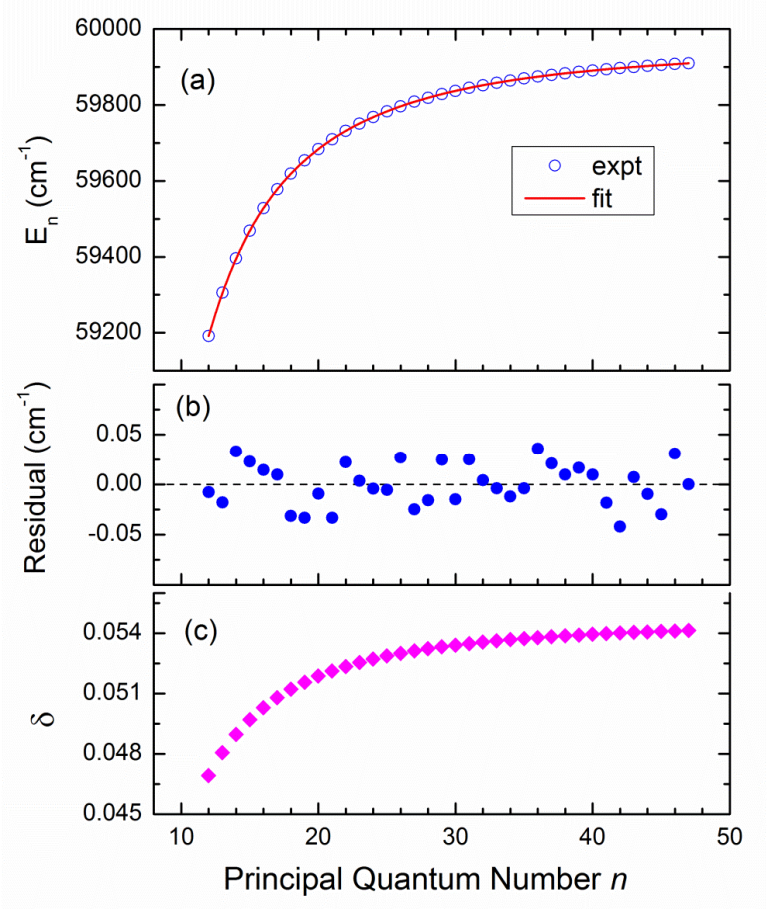

Figure 4. (a) Rydberg-Ritz fit for the *nf* $^6F^\circ$ series, (b) the corresponding residuals with experimental data, and (c) the calculated quantum defects using Eq. (6).

Table 2. Members of the *nf* $^6F^o_{9/2,7/2,5/2}$ series converging to the ground state of Mn II.

n	E_n (expt) (cm^{-1})	E_n (fit)(cm^{-1})	δ(n)
12	59191.50(21)	59191.51	0.04691
13	59305.39(25)	59305.41	0.04806
14	59395.78(23)	59395.74	0.04897
15	59468.62(30)	59468.60	0.04970
16	59528.21(25)	59528.19	0.05030
17	59577.58(34)	59577.57	0.05080
18	59618.90(19)	59618.93	0.05121
19	59653.89(26)	59653.92	0.05156
20	59683.78(30)	59683.79	0.05186
21	59709.45(25)	59709.49	0.05212
22	59731.77(20)	59731.75	0.05235
23	59751.17(29)	59751.17	0.05254
24	59768.20(24)	59768.21	0.05271
25	59783.23(30)	59783.24	0.05286
26	59796.59(24)	59796.56	0.05300
27	59808.41(25)	59808.44	0.05312
28	59819.04(25)	59819.06	0.05322
29	59828.62(24)	59828.60	0.05332
30	59837.18(23)	59837.20	0.05341
31	59845.00(28)	59844.98	0.05348
32	59852.04(30)	59852.04	0.05355
33	59858.46(23)	59858.46	0.05362
34	59864.32(29)	59864.33	0.05368
35	59869.70(30)	59869.70	0.05373
36	59874.67(21)	59874.63	0.05378
37	59879.19(24)	59879.17	0.05383
38	59883.36(31)	59883.35	0.05387
39	59887.23(28)	59887.21	0.05391
40	59890.80(30)	59890.79	0.05394
41	59894.09(14)	59894.11	0.05398

42	59897.15(30)	59897.19	0.05401
43	59900.07(15)	59900.06	0.05404
44	59902.73(23)	59902.74	0.05406
45	59905.21(33)	59905.24	0.05409
46	59907.61(29)	59907.58	0.05411
47	59909.77(26)	59909.77	0.05413

The spectrum shown in Fig. 3 was measured when the ion source was heated with electric currents of 235 A for the cavity and 350 A for the target reservoir, at which the average cavity temperature was estimated to be about 1500 °C. At higher ion source temperatures, a second, very weak series started to appear at the left side of the *nf* ^{6}F° series, as shown in Fig. 5. Moreover, the weak and broad structure on the right side of the *nf* ^{6}F° peaks, which consisted of several partially resolved components, became more visible. The structure next to the 12*f* ^{6}F° peak consisted of five partially resolved peaks. The two small peaks immediately next to the main peak are centered at 59193.61(28) cm^{-1} and 59194.29(28) cm^{-1}, respectively, in excellent agreement with the values of 59193.78 cm^{-1} for the 14*p* ^{6}P°$_{7/2}$ state and 59194.28 cm^{-1} for the 14*p* ^{6}P°$_{5/2,3/2}$ state as reported in Ref. [26]. The energies and relative intensities of these two peaks suggest that they correspond to the electric dipole-allowed 3d^{5}4s4d *e* ^{6}D$_{7/2}$ → 3d^{5}4s (^{7}S)14*p* ^{6}P°$_{7/2,5/2}$ transitions. This also supports the assignment that the intense peaks belongs to the *nf* ^{6}F°$_{9/2,7/2,5.2}$ series. The weak *np* ^{6}P°$_{7/2,5/2}$ transitions were no longer resolvable from the broad features for *n* > 18.

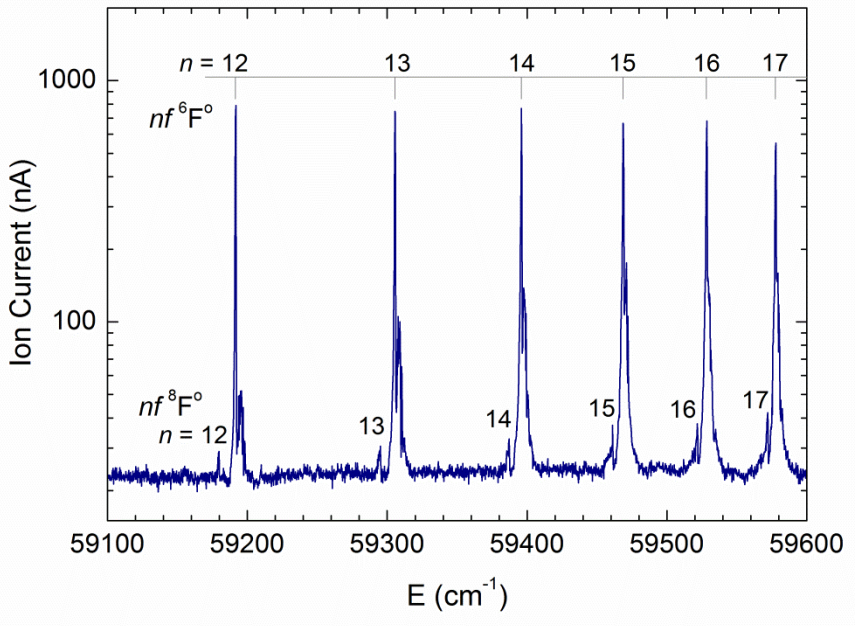

Figure 5. Rydberg spectrum observed at source heating currents of 276 A for the cavity and 450 A for the reservoir, with estimated average cavity temperature of about 1900 °C. The weak *nf* ^{8}F° peaks can be seen on the left side of the *nf* ^{6}F° series.

The newly observed weak peaks at the left side of the *nf* ^{6}F° series have been determined to be the members of the semi-forbidden *nf* ^{8}F°$_{9/2,7/2,5/2}$ series, with multiplet splittings not resolved, converging to

the ground state of Mn II. This assignment is based on the observed energetic orders: the *nf* ^{8}F° levels were lower in energy than both the corresponding *nf* ^{6}F° levels as well as the known *np* ^{8}P° series reported in Ref. [26]. About 19 members (n = 12-30) of the *nf* ^{8}F° series were identified. A convergence limit of E_{limit} = 59958.98 ± 0.16 cm^{-1} with δ_0 = 0.2024 ± 0.0037 is obtained by fitting, which is smaller than the expected IP of Mn. This disagreement may be attributed to limited number of ^{8}F° levels available for the fitting. The experimental and fitted energies of the observed *nf* ^{8}F° levels are given in Table 3.

Table 3. Members of the *nf* $^8F^o_{9/2,7/2,5/2}$ series converging to the ground state of Mn II.

n	E_n (expt) (cm^{-1})	E_n (fit) (cm^{-1})	δ(n)
12	59178.87(30)	59178.85	0.13983
13	59294.45(7)	59294.48	0.14923
14	59386.45(2)	59386.36	0.15667
15	59460.31(49)	59460.51	0.16264
16	59521.29(16)	59521.20	0.16752
17	59571.57(16)	59571.49	0.17156
18	59613.55(33)	59613.61	0.17493
19	59649.20(28)	59649.23	0.17778
20	59679.53(28)	59679.63	0.18021
21	59705.74(13)	59705.77	0.18229
22	59728.51(41)	59728.41	0.18410
23	59748.26(42)	59748.15	0.18567
24	59765.54(18)	59765.46	0.18705
25	59780.86(26)	59780.73	0.18827
26	59794.39(24)	59794.26	0.18935
27	59806.23(32)	59806.31	0.19030
28	59817.04(39)	59817.08	0.19116
29	59826.69(32)	59826.75	0.19193
30	59835.29(30)	59835.47	0.19262

3.3. Autoionizing states

Three-step excitation into the continuum was carried out to investigate the energy range of 61300 to 62750 cm^{-1} for strong AI resonances. Figure 6 shows the corresponding photoionization spectrum, which was obtained by scanning the third step wavelength between 750 nm and 841 nm, while the first and second lasers were fixed in resonance for the excitation sequence of $a\ ^6S_{5/2} \rightarrow y\ ^6P^o_{7/2} \rightarrow f\ ^6S_{5/2}$, according to the pathway on the left in Fig. 1. The spectrum is plotted as function of the total photon energy, which is the sum of the third photon energy and the energy of the $3d^54s5s\ f\ ^6S_{5/2}$ state. In the excitation from this final intermediate state a number of AI resonances were observed. The dominant feature of the spectrum

is the intense and broad structure at around 62000 cm^{-1}, which consists of several overlapping AI resonances, together with the strong and narrow peaks around 62070 cm^{-1}. Figure 7 shows the details of these AI structures observed between 61400 cm^{-1} and 62100 cm^{-1}, with the substructures and a number of weak peaks located below 62000 cm^{-1} shown in Fig. 7(a) as magnified by a factor of ten.

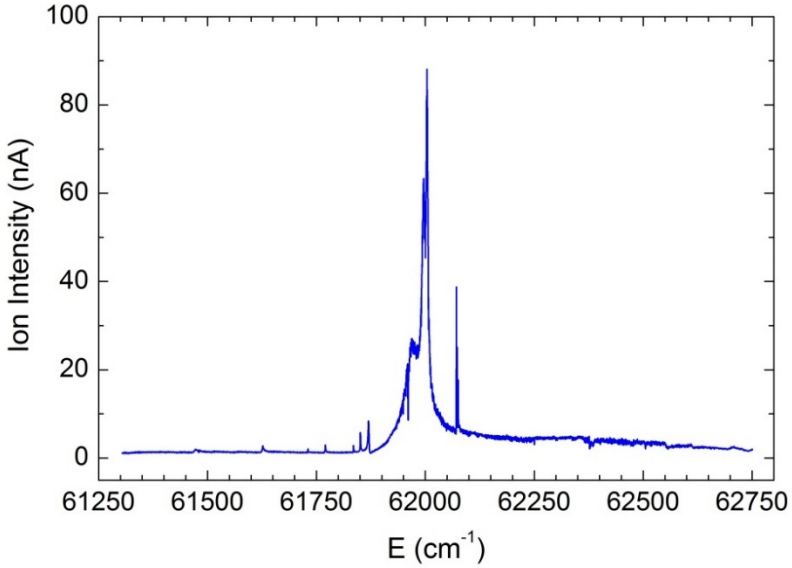

Figure 6. Autoionization spectrum of Mn obtained by scanning the third laser wavelength over the tuning range of 750 - 841 nm. The first two excitation steps were $a\ ^6S_{5/2} \rightarrow y\ ^6P^o_{7/2} \rightarrow f\ ^6S_{5/2}$. The spectrum is plotted as function of the total photon energy.

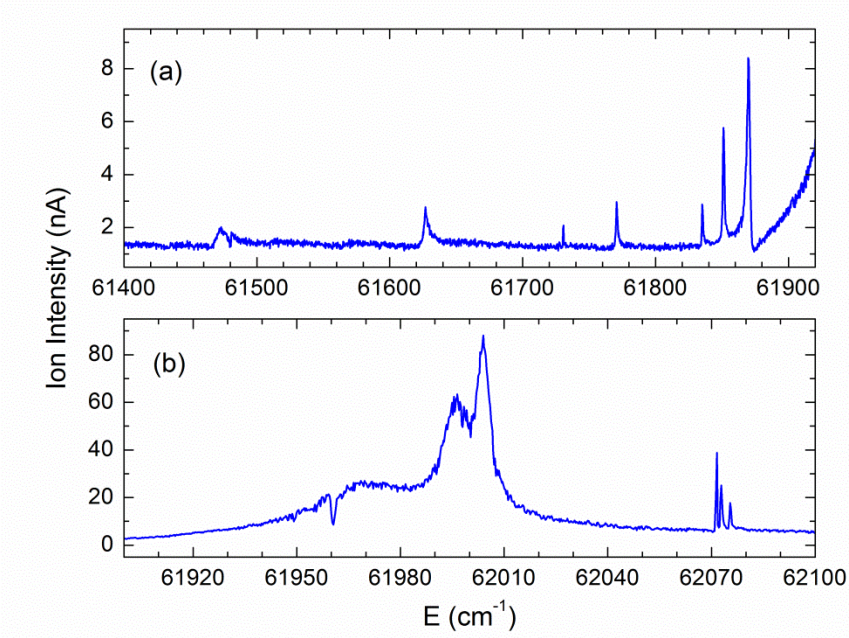

Figure 7. Portions of the spectrum in Fig. 6, showing the details of the AI resonances. Note the different vertical scaling of the plots with ten times magnification for the upper one.

Most of the AI resonances clearly exhibit asymmetric profiles, which may arise from the interaction of the AI states and the continuum. Thus, individual AI resonances are fitted with the Fano profile [28,29] of the form

$$I(E) = a\,\frac{(q\frac{\Gamma}{2}+E-E_r)^2}{(E-E_r)^2+(\frac{\Gamma}{2})^2} + b, \tag{7}$$

where I(E) is ion intensity at total photon energy E, E_r is the resonance energy, Γ is the width of the resonance, q is the asymmetry parameter, and a and b are amplitude parameters associated with the resonant and the non-resonant contributions, respectively. Overlapping resonances are assumed to be uncoupled AI states interacting with the multiple continuum states and are fitted to a superposition of the Fano profiles as given by

$$I(E) = \sum_i a_i \frac{(q_i\frac{\Gamma_i}{2}+E-E_{ri})^2}{(E-E_i)^2+(\frac{\Gamma_i}{2})^2} + b\,, \tag{8}$$

where E_{ri}, q_i, Γ_i, and a_i are as in Eq. (7), related to the i^{th} AI resonance, while b represents the non-resonant background.

The dominant AI feature at around 62000 cm^{-1} is composed of one destructive and three positive overlapping resonances. As shown in Fig. 8, the experimental spectrum can be fitted to Eq. (8) with i = 1 to 4, assuming four AI states interacting with the continuum. The resonance energy E_r, asymmetry parameter q, and the width Γ of the four Fano resonances are given in Table 4, as obtained from the Fano fits of several experimental measurements of the same spectral region. It is postulated that the two strong resonances at 62000 cm^{-1} are associated with the electric dipole-allowed transitions $3d^54s5s\ f\ ^6S_{5/2} \rightarrow 3d^54s6p\ ^6P^\circ_{7/2,5/2,3/2}$ as denoted in pure Russell-Saunders coupling. However, in the literature only one level, incompletely assigned as $3d^54s(^5S)6p\ ^6P^\circ$ and located at 61870.6 cm^{-1}, is given [23]. This energetic position agrees well with the strongest peak below 61900 cm^{-1} [Fig.7(a)], which nevertheless appears almost insignificant against the structure centered around 62000 cm^{-1}. Correspondingly, a proper assignment of the various structures observed could not be obtained and requires a detailed theoretical analysis.

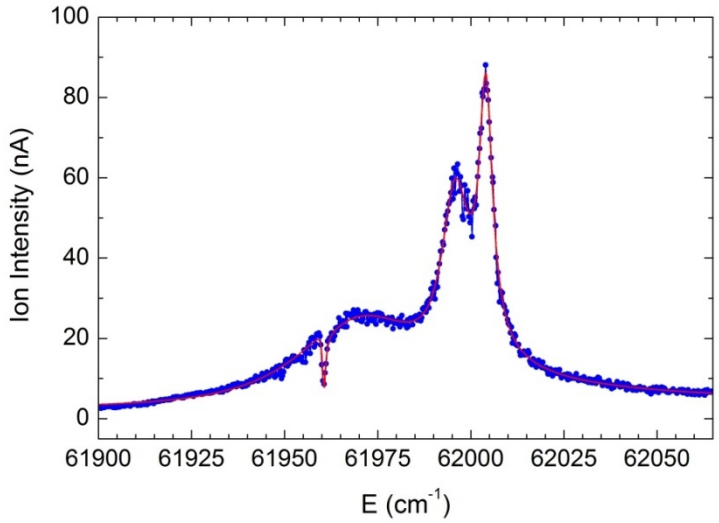

Figure 8. The line profile of the strong autoionization resonances observed. The solid line is the fit of Eq. (8) for a superposition of four Fano profiles.

Table 4. The E_r, q, and Γ parameters of the four AI states in the strongest autoionization region shown in Figs. 8 and 7(b).

E_r (cm^{-1})	q	Γ (cm^{-1})
61960.1(4)	-0.27(5)	1.1(1)
61968(1)	9(1)	42(2)
61995.4(4)	13(3)	8.6(2)
62003.8(2)	40(15)	4.23(8)

In addition to the dominant feature discussed above, about a dozen of weak AI resonances were observed below and above the strong structure. The experimentally observed spectral profiles of these weak resonances have also been analyzed using Eqs. (7) and (8). Figure 9 presents two examples of the Fano fits to the experimental data. Table 6 lists the resonance energies of all the weak AI resonances obtained from such analyses. The relative intensities of these AI transitions can be inspected in Figs. 6 and 7. Once again, the photoionization spectrum alone is not sufficient to allow for term assignments for these AI states. Brown and Ginter [26] have observed many AI levels in absorption spectra, which correspond to transitions from the $3d^5 4s^2$ a $^6S_{5/2}$ ground state of neutral Mn. It is noticed that all the weak AI resonances observed in this work could be matched rather well to the AI lines in Ref. [26], while the dominant resonances shown in Fig. 8 have not been reported before. This is somewhat unexpected, as the initial configuration for the AI excitation in this work, $3d^5 4s5s$ $^6S_{5/2}$, is identical to that in [26], except for the principal quantum number of one electron. The differences must thus be ascribed to configuration admixtures in the rather high lying level $3d^5 4s5s$ $^6S_{5/2}$, located at 49415.35 cm^{-1}. In Table 5 the positions of these weak resonances are given and compared to previously identified AI levels, for which known assignments are included. From this we may conclude that most of the weak AI resonances correspond to electric dipole-forbidden transitions. As in the case of the nf $^8F^\circ$ Rydberg series, their appearance in our measurement is ascribed to the fact that the ion source was operated at high temperatures, favoring population of high levels and corresponding level admixtures.

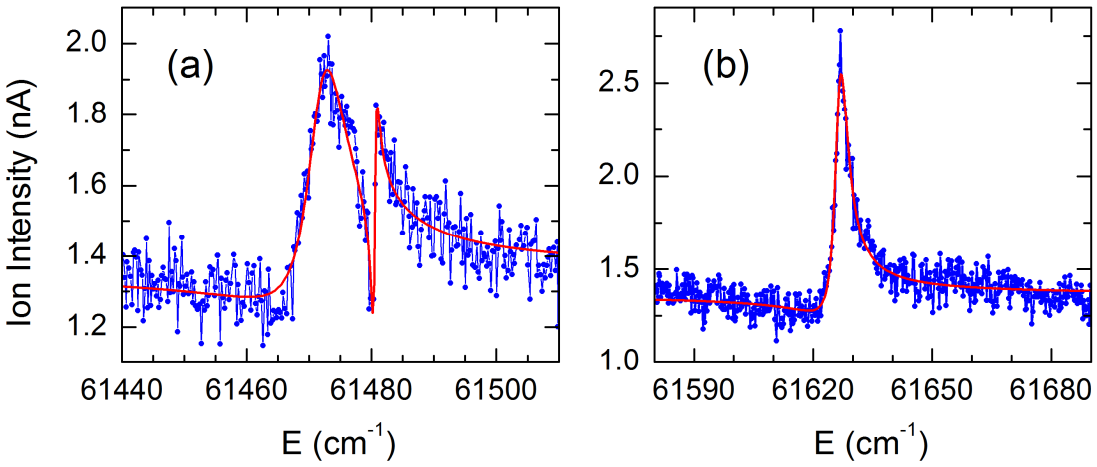

Figure 9. Two weak AI resonances observed between 61440 cm^{-1} and 61700 cm^{-1}. The experimental data are fitted to (a) Eq. (8), giving E_{r1} = 61470.4(18) cm^{-1}, q_1 = 3.1(2), Γ_1 = 7.8(4) cm^{-1}, E_{r2} = 61480.46(8) cm^{-1}, q_2 = 0.8(1), and Γ_2 = 0.7(1) cm^{-1}; (b) Eq. (7) with E_r = 61626.3(3) cm^{-1}, q = 3.8(2), and Γ = 4.0(1). Solid lines represent the fitted Fano profiles.

Table 5. Weak AI resonances observed in this work, compared with previously reported AI levels in Mn.

E_r (cm^{-1})	Ref. [26,23] (cm^{-1})	Assignment[26]
61470.4(18)	61469.7	$3d^6\ (a^3F)4p\ ^2F^o_{5/2}$
61480.46(8)	61480.6	$3d^6\ (a^3F)4p\ ^2F^o_{7/2}$
61626.3(3)	61625.8	
61730.2(4)	61730.16	
61770.4(3)	61770.1	
61834.8(3)	61834.55	
61850.8(4)	61850.4	
61870.0(3)	61870.6	$3d^5\ 4s(^5S)6p\ ^6P^o$
62071.3(2)	62071.3	
62072.6(2)	62073.13	
62075.2(3)	62075.55	$3d^6\ (^3G)4p\ ^4G^o_{5/2}$

3.4 Properties of the three-photon resonant ionization of Mn

As shown in Fig. 1, three-photon resonance excitation and ionization of neutral Mn atoms using Ti:sapphire lasers can be achieved with a number of atomic excitation schemes, involving different intermediate states and Rydberg states or alternatively AI states in the last ionization step. For laser ion source applications high ionization efficiency is desirable, which in turn requires the saturation of all excitation steps involved. Hence, we have studied both, the laser powers needed to saturate the various excitations and finally the overall ionization efficiency, which could be obtained for Mn in the hot cavity RILIS.

3.4.1. Saturation power

Figure 10 shows the measured Mn ion intensities as a function of the laser power for schemes involving an AI state in the last step. Two different first steps, $a\ ^6S_{5/2} \rightarrow y\ ^6P^o_{7/2}$ and $a\ ^6S_{5/2} \rightarrow y\ ^6P^o_{5/2}$ transitions, were compared. The excited Mn atoms were further lifted to the $3d^5 4s5s\ f\ ^6S_{5/2}$ state at 49415.35 cm^{-1} in the second step and then in the third step to the largest AI resonance, located at 62003.8 cm^{-1}. The ion intensities shown were determined by the ion source operating conditions as well as the amount of Mn sample in the ion source, not reflecting the relative ionization efficiency of the different excitation schemes. The experimental data are fitted to the following saturation formula

$$I = I_0 + A\frac{P/P_{sat}}{P/P_{sat}+1}, \tag{9}$$

where I is the ion current, P is the laser power, P_{sat} is the saturation power, I_0 is the background ion current, and A is an amplitude parameter. For the first excitation steps, the third harmonics generation

(THG) of the fundamental Ti:sapphire laser output was required, which was limited in power to about 30 mW at ~280 nm. Of the two first steps, the $a\ ^6S_{5/2} \rightarrow y\ ^6P^o_{7/2}$ transition was not fully saturated with the available THG power of 22 mW, while the $a\ ^6S_{5/2} \rightarrow y\ ^6P^o_{7/2}$ transition shows strong saturation already from 5 mW laser power on. This is confirmed by the observed line profiles presented in Figs. 2(a) and (b): a Voigt line shape for the $a\ ^6S_{5/2} \rightarrow y\ ^6P^o_{7/2}$ transition and a saturated Gaussian line shape for the $a\ ^6S_{5/2} \rightarrow y\ ^6P^o_{5/2}$ transition. On the other hand the finding is inconsistent with the rather identical transition strengths of the two transitions with A_{ki} factors around 3.6 x10^8 s^{-1} [23] and might have been caused by some experimental shortcoming. As shown in the lower graphs of Fig. 11, the second and third steps with wavelengths between 790 nm and 860 nm could once again be well saturated with less than 1 W power of the fundamental output of the Ti:sapphire lasers. Figure 11 shows the saturation data for the second and third steps of the scheme involving a Rydberg state: $a\ ^6S_{5/2} \rightarrow y\ ^6P^o_{5/2} \rightarrow e\ ^6D_{5/2} \rightarrow$ Rydberg state, where the Rydberg state was the n = 13 member of the $^6F^\circ$ series observed. Also these two transitions could be strongly saturated. Table 6 summarizes the P_{sat} values obtained for the transitions. Due to limited time, not all the transitions shown in Fig. 1 were studied, but the data obtained so far indicate that the ionization schemes demonstrated can be saturated with practical laser power.

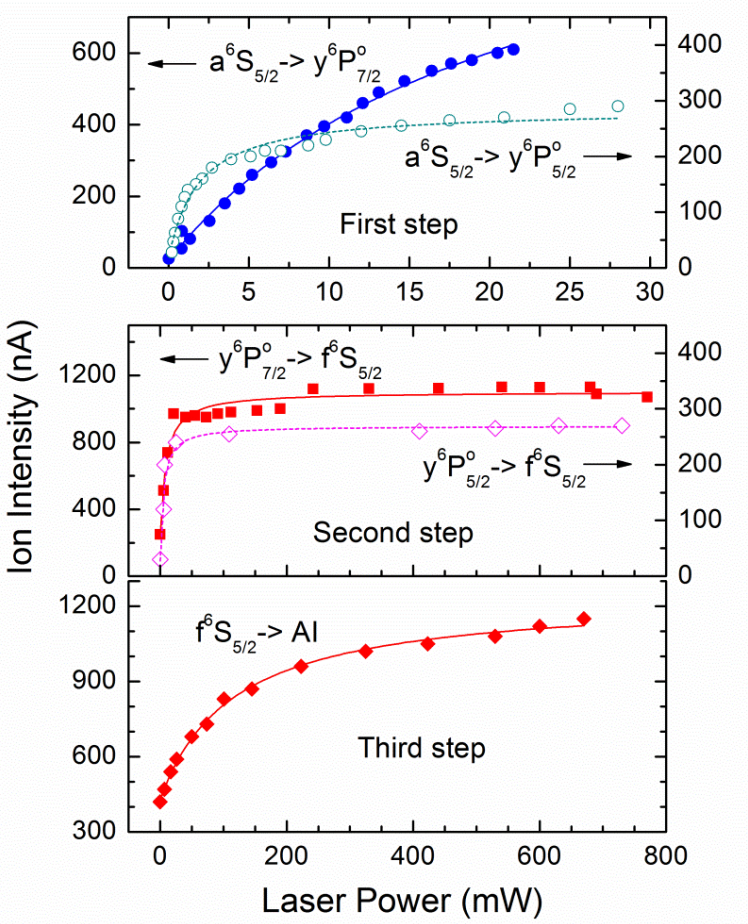

Figure 10. Saturation data for the first excitation $a\ ^6S_{5/2} \rightarrow y\ ^6P^o_{7/2}$, second excitation $y\ ^6P^o_{7/2} \rightarrow f\ ^6S_{5/2}$, and third excitation to the AI at ~62003 cm^{-1}. The points are the measured ion intensities; the solid lines are the fits to Eq. (9).

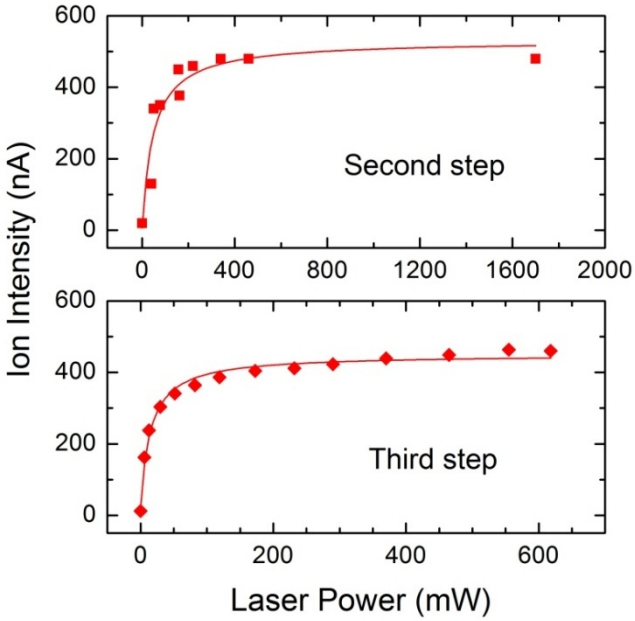

Figure 11. Saturation data for the second excitation $y\ ^6P^o_{5/2} \rightarrow e\ ^6D_{5/2}$ and third excitation to a Rydberg state ($13f\ ^6F^\circ$). The points are measured ion intensities; the solid lines are the fits to Eq. (9).

Table 6. Saturation power P_{sat} for different ionization schemes.

Scheme	P_{sat} (λ_1) (mW)	P_{sat} (λ_2) (mW)	P_{sat} (λ_3) (mW)
$a\ ^6S_{5/2} - y\ ^6P^o_{7/2} - f\ ^6S_{5/2}$ – AI	22(2)	9(2)	116(9)
$a\ ^6S_{5/2} - y\ ^6P^o_{5/2} - f\ ^6S_{5/2}$ – AI	1.8(3)	5(1)	116(9)
$a\ ^6S_{5/2} - y\ ^6P^o_{5/2} - e\ ^6D_{5/2}$ – Rydberg	1.8(3)	49(20)	15(2)

3.4.2 Ionization efficiency

The overall ionization efficiency of the RILIS for Mn was measured for two excitation schemes, one employing a Rydberg state and the other one using an AI state in the third step. For the former, the $a\ ^6S_{5/2} \rightarrow y\ ^6P^o_{5/2} \rightarrow e\ ^6D_{5/2} \rightarrow$ Rydberg scheme was applied, with the third laser tuned to the strongest Rydberg peak. For the latter, the $a\ ^6S_{5/2} \rightarrow y\ ^6P^o_{3/2} \rightarrow f\ ^6S_{5/2} \rightarrow$ AI at 62003 cm^{-1} scheme was tested because this excitation sequence seemed to yield relatively higher Mn ion current. To measure the absolute ionization efficiency, a quantified sample containing 10^{17} atoms of ^{55}Mn was placed into the hot cavity ion source. The ion source was slowly heated to maximum temperature, gradually evaporating the Mn sample and releasing gaseous Mn atoms, while the laser beams were kept in resonance for the selected excitations. The Mn ion current extracted from the ion source was continuously recorded until it dropped below 1-2 nA while the ion source was heated to high temperatures and further heating did not increase the ion current, which was considered as the indication that the sample materials were mostly evaporated and effused out of the source. The ionization efficiency was calculated as the ratio of the integrated total number of detected ions to the total number of neutral atoms initially in the sample. A

rather low ionization efficiency of about 0.3% was obtained for the scheme using Rydberg state excitation. Two efficiency measurements for the AI scheme were performed, both consistently yielding an efficiency of about 0.9%. The results indicate that ionization via the AI state was more efficient.

The overall ionization efficiency for Mn obtained in this study is generally much lower than expected. A value of 4.8% was reported by Fedoseyev et al. [6] with a tungsten hot cavity RILIS, who used the identical first step into the $y\ ^6P^o_{5/2}$ level with similar laser powers, a second non-saturated excitation into the $3d^7\ e\ ^4P_{5/2}$ level by 628.270 nm dye laser radiation, and subsequent high power ionization with 7.5 W of the 510.6 nm radiation from a copper vapor laser. The last transition was assumed by the authors to accidentally hit an AI to explain the much higher efficiency than other excitation ladders [6]. Inspecting the Mn ion intensities recorded during the efficiency measurements, we noticed that the Mn ion current reached a maximum of near 40 nA in a very short time at relatively low temperatures and then decreases monotonically – further increasing the ion source temperature did not increase the Mn ion current as expected. In less than three hours, the Mn ion intensity dropped by about a factor of 20 to only 1-2 nA and stayed at such low levels. In Fig. 12 the Mn efficiency data is compared to that of Sn measured under similar conditions: about 10^{17} atoms were inserted into a hot cavity RILIS and a three-photon resonance ionization scheme was applied. An ionization efficiency of about 22% was obtained for Sn [20]. In contrast to Mn, the Sn efficiency data exhibit sustained high ion currents, requiring altogether about 8 hours to deplete the sample. Comparing the Mn and Sn behaviors, we conclude that the ionization efficiency for Mn may not be limited by the laser photoionization process but by reactions of the Mn atoms with the ion source surfaces. At sufficiently high temperatures, atomic Mn may reacted with or diffuse into tantalum or other ion source materials. This assumption is supported by the significantly higher but still not ideal RILIS efficiency quoted in [6]. The latter was obtained within a hot tungsten cavity, which seemingly did not foster those reactions in a similar way. Hence, improvements in the material properties of the ion source and possibly its overall geometrical layout as well as operation conditions could lead to significant improvements in the achievable ionization efficiency for Mn with our hot cavity RILIS. Corresponding developments are in progress.

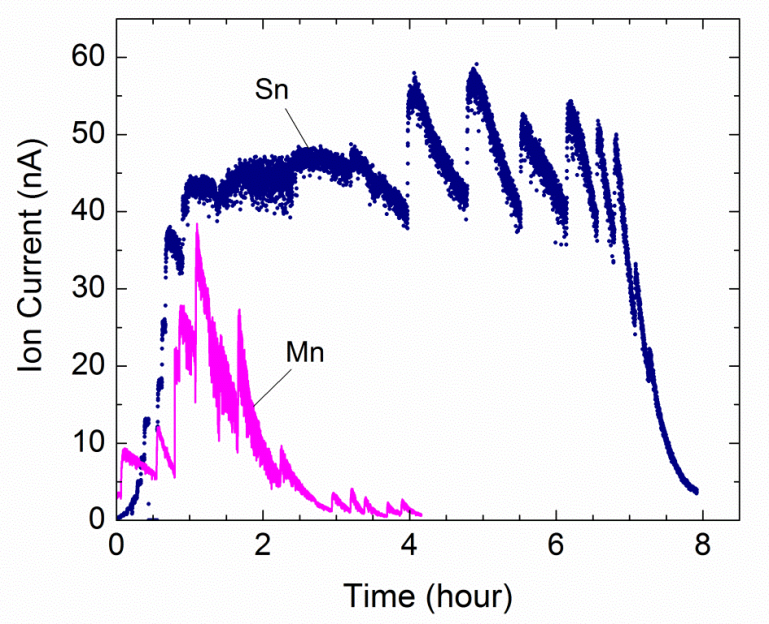

Figure 12. A comparison of the efficiency measurement data recorded for Mn and Sn using calibrated samples containing 10^{17} atoms of interest. The sharp jumps in the ion intensities correspond to stepwise increases in the ion source heating current. The corresponding ionization efficiency was about 0.9% for Mn and 22% for Sn.

4. Conclusion

Three-photon resonance ionization of atomic Mn using tunable Ti:sapphire lasers in a hot cavity laser ion source was demonstrated for the first time. Different three-step resonant excitation and ionization schemes involving Rydberg or alternatively AI states in the final step have been studied. Neutral Mn atoms were excited from the ground state to the $3d^5 4s4p\ y\ ^6P^o_{7/2,\ 5/2,\ 3/2}$ excited states by frequency-tripled photons of $\lambda_1 \sim 280$ nm. In the second step, Mn atoms could be promoted by an infrared photon to the $3d^5 4s4d\ e\ ^6D_{9/2,7/2,\ 5/2}$ states at 47207.28 cm^{-1}, 47212.06 cm^{-1}, and 47215.61 cm^{-1}, respectively ($\lambda_2 \sim 870$-874 nm) or to the $3d^5 4s5s\ f\ ^6S_{5/2}$ state at 49415.35 cm^{-1} ($\lambda_2 \sim 728$-732 nm). Laser spectroscopic investigations in the third step revealed suitable Rydberg series and strong AI resonances that may be employed for resonant ionization. The Rydberg levels were accessible from the $3d^5 4s4d\ e\ ^6D_{92,\ 7/2,\ 5/2}$ intermediate states, while the AI resonances could be reached from the $3d^5 4s5s\ f\ ^6S_{5/2}$ state.

Rydberg levels associated with the $3d^5 4s4d\ e\ ^6D_{7/2}$ intermediate level were analyzed in detail. An intense Rydberg series was identified as the electric dipole-allowed $nf\ ^6F^\circ_{9/2,7/2,5/s}$ (n = 12-47) series converging to the ground state of the ion Mn II. From the Rydberg series, the ionization potential of Mn was determined as 59959.56 ± 0.01 cm^{-1}, enhancing precision of this value by about a factor of 10. When the ion source was operated at relatively high temperatures, a very weak series at energies below the $nf\ ^6F^\circ$ series was visible and was assigned to the semi-forbidden $nf\ ^8F^\circ_{9/2,7/2,5/2}$ (n = 12-30). Furthermore, more than ten AI resonances have been observed between 61400 cm^{-1} and 62100 cm^{-1}. The most intense AI feature, located at about 62000 cm^{-1}, could be described by four AI states interacting with the continuum. To our knowledge, these strong AI resonances have not been previously reported. The other weaker AI resonances match with those reported in Ref. [26].

The efficiency of ionizing Mn in the hot cavity RILIS was studied using two different three-step ionization schemes. One scheme leads to the most intense AI resonance; the other scheme reaches a strong Rydberg transition. The overall ionization efficiency obtained was about 0.9% for the former and 0.3% for the latter. However, the experimental data indicate that the achievable ionization efficiency was limited by the interaction of Mn atoms with the ion source material, predominantly tantalum, at high temperatures, rather than the process of photoionization. Therefore, significantly higher efficiency is expected by involving appropriate techniques to reduce surface or bulk interactions with atomic Mn in the ion source.

Acknowledgements

This material is based upon work supported by the U.S. Department of Energy, Office of Science, Office of Nuclear Physics and the German Bundesministerium für Bildung und Forschung under Grant 06MZ215. This research used resources of the Holifield Radioactive Ion Beam Facility of Oak Ridge National Laboratory, which was a DOE Office of Science User Facility.

References

1. F.C. Charlwood, J. Billowes, P. Campbell, B. Cheal, T. Eronen, D.H. Forest, S. Fritzsche, M. Honma, A. Jokinen, I.D. Moore, H. Penttilä, R. Powis, A. Saastamoinen, G. Tungatec, J. Äystö, Phys. Lett. B 690 (2010) 346-351.

2. M. Hannawald, T. Kautzsch, A. Wöhr, W. B. Walters, K.-L. Kratz, V. N. Fedoseyev, V. I. Mishin, W. Böhmer, B. Pfeiffer, V. Sebastian, Y. Jading, U. Köster, J. Lettry, H. L. Ravn, and the ISOLDE Collaboration, Phys. Rev. Lett. 82 (1999) 1391-1394.

3. A. Herlert, S. Van Gorp, D. Beck, K. Blaum, M. Breitenfeldt, R.B. Cakirli, S. George, U. Hager, F. Herfurth, A. Kellerbauer, D. Lunney, R. Savreux, L. Schweikhard, and C. Yazidjian, Eur. Phys. J. A 48, 97 (2012).

4. S. Naimi, G. Audi, D. Beck, K. Blaum, Ch. B¨ohm, Ch. Borgmann, M. Breitenfeldt, S. George, F. Herfurth, A. Herlert, A. Kellerbauer, M. Kowalska, D. Lunney, E. Minaya Ramirez, D. Neidherr, M. Rosenbusch, L. Schweikhard, R. N. Wolf, and K. Zuber, Phys. Rev. C 86, 014325 (2012).

5. J. Van de Walle, et al. Eur. Phys. J. A **42** (2009) 401–406.

6. V.N. Fedoseyev, K. Btitzner, R. Catherall, A.H.M. Evensen, D. Forkel-Wirth, O.C. Jonsson, E. Kugler, J. Lettry, V.I. Mishin, H.L. Ravn, G. Weyer , the ISOLDE Collaboration, Nucl. Instr. and Meth. B 126, (1997) 88-91.

7. Y. Kobayashi, AIP Conf. Proc. 1120, 215 (2009).

8. U. Wahl, Nucl. Instr. Meth. B 269 (2011) 3014-256.

9. L. M. C. Pereira, U. Wahl, S. Decoster, J. G. Correia, L. M. Amorim, M. R. da Silva, J. P. Araújo and A. Vantomme, Phy.Rev. B 84, 125204 (2011).

10. M.R. Silva, U. Wahl, J.G. Correia, L.M. Amorim and L.M.C. Pereira, Rev. Sci. Instru. 84, 073506 (2013).

11. S. Decoster, S. Cottenier, U. Wahl, J. G. Correia, L. M. C. Pereira, C. Lacasta, M. R. Da Silva, and A. Vantomme, Appl. Phys. Lett. 97, 151914 (2010).

12. E. Rita, U. Wahl, J. G. Correia, E. Alves, and J. C. Soares, Appl. Phys. Lett. 85, 4899 (2004).

13. V. N. Fedosseev, Yu Kudryavtsev and V. I. Mishin, Phys. Scr. 85, 058104 (2012).

14. B.A. Marsh, L.-E. Berg, D.V. Fedorov, V.N. Fedosseev, O.J. Launila, M. Lindroos, R. Losito, F.K. Österdahl, T. Pauchard, I.T. Pohjalainen, U. Sassenberg, M.D. Seliverstov, A.M. Sjödin, G. Tranströmer, Hyperfine Interact. **196** (2010) 129-141.

15. E.B. Saloman, Spectrochimica Acta **49B** (1994) 251-281.

16. J. Lassen, P. Bricault, M. Dombsky, J. P. Lavoie, Ch. Geppert and K. Wendt, Hyperfine Interact. 165 (2005) 69–75.

17. Y. Liu, C.U. Jost, A.J. Mendez II, D.W. Stracener, C.L. Williams, C.J. Gross, R.K. Grzywacz, M. Madurga, K. Miernik, D. Miller, S. Padgett, S.V. Paulauskas, K.P. Rykaczewski, M. Wolinska-Cichocka, Nucl. Instr. and Meth. B **298** (2013) 5-12.

18. A. Nieminen, *et al. Hyperfine Interact.* **162** (2005) 39–43.

19. N. Lecesne, *et al. Rev.Sci. Instrum.* **81** (2010) 02A910.

20. Y. Liu, C. Baktash, J. R. Beene, H. Z. Bilheux, C. C. Havener, H. F. Krause, D. R. Schultz, D. W. Stracener, C. R. Vane, K. Brück, Ch. Geppert, T. Kessler, K. Wendt, Nucl. Instr. and Meth. B 243, 442 (2006).

21. T. Kessler, K. Brück C. Baktash, J. R. Beene, Ch. Geppert, C. C. Havener, H. F. Krause, Y. Liu, D. R. Schultz, D. W. Stracener, C.R. Vane, and K. Wendt, J. Phys. B: At. Mol. Opt. Phys. 40 (2007) 4413-4432.

22. C. Geppert, P. Bricault, R. Horn, J.Lassen, C. Rauth and K. Wendt, Nucl. Phys. A **746** (2004) 631c.

23. http://www.nist.gov/pml/data/asd.cfm/

24. J.F. Kielkopf, J. Opt. Soc. Am. 63 (1973) 987.

25. S. Bruce, J. Higinbotham, I. Marshall, P. Beswick, J. Magn. Reson. 142 (2000) 57.
26. C.M. Brown, M.L. Ginter, J. Opt. Soc. Am. 68 (1978) 1541.
27. W. Ritz, *Phys. Z.* **4** (1903) 406.
28. K. Ueda, Phys. Rev. A 35 (1987) 2484.
29. U. Fano, J.W. Cooper, Phys. Rev. 137 (1965) A1364.